Paper C

Numerical studies of nonhydrostatic pressure effects on the wind forced boundary layer dynamics *

* *BCCS Technical report series.*

BCCS
TECHNICAL REPORT SERIES

Numerical studies of nonhydrostatic pressure effects on wind forced boundary layer dynamics

Bergh, J., Berntsen, J.

REPORT No. 25 **October 2009**

UNIFOB
the University of Bergen research company

BERGEN, NORWAY

BCCS Technical Report Series is available at http://www.bccs.no/publications/

Requests for paper copies of this report can be sent to:

Bergen Center for Computational Science, Høyteknologisenteret,
Thormøhlensgate 55, N-5008 Bergen, Norway

Abstract

With increasing computer capacity numerical ocean models are used with higher and higher resolution. The hydrostatic approximation will no longer be valid and the influence of nonhydrostatic pressure effects should be considered. Internal waves may be generated, directly or indirectly, by the wind or the tide. Nonhydrostatic pressure effects will be important for propagating nonlinear internal waves. However, the role of the nonhydrostatic pressure in the generation phase of internal waves is more unclear.

In the present study a numerical ocean model with nonhydrostatic capacity is used to study the generation phase of wind induced internal waves in a simplified system. The influence of nonhydrostatic pressure will depend on the resolution, and we are therefore running the model with increasing horizontal resolution and comparing the results from a hydrostatic and a nonhydrostatic model.

The results show that the strength of the nonhydrostatic pressure grow when the grid scale is reduced in all calculations. The nonhydrostatic pressure does not influence the results significantly during the generation phase using a grid resolution of $25\,\mathrm{m}$ or larger. With a horizontal resolution of $12.5\,\mathrm{m}$, both the density field and the velocity field are influenced by the nonhydrostatic pressure. Instabilities are generated at the rear end of the wave in all calculations. The instabilities are restricted to an area close to the boundary with a grid resolution of $25\,\mathrm{m}$ and larger. Though, in the nonhydrostatic calculation with a grid resolution of $12.5\,\mathrm{m}$, the instabilities are transported further into the model domain and a larger area is accordingly influenced by mixing. This is not seen in the hydrostatic results. The results with a horizontal resolution of $12.5\,\mathrm{m}$ indicate that the small scale physical processes are not fully resolved. With higher resolution these processes may be better represented and the strength of the nonhydrostatic pressure may further increase.

1 Introduction

Most of the numerical ocean models used in the scientific community apply the hydrostatic approximation. This approximation results in a more simple form of the momentum equations and a set of equations that are more efficient to solve. In most ocean scale studies, when the horizontal scales and motions are much larger then the vertical scales and motions, a hydrostatic model gives trustworthy results. Though, when modelling physical processes on scales less than 1-10 km, the physical processes excluded in a hydrostatic model may be of importance [Marshall et al., 1997, Gill, 1982]. High resolution ocean models, with horizontal grid resolution of 1 km and less, are needed today in studies of the coastal ocean and to study specific physical phenomena in the open ocean. In these studies, nonhydrostatic pressure effects have to be considered, and the models capacity to capture the nonhydrostatic pressure effects will be of vital importance.

In recent years research groups are in the process of developing ocean models with the capacity to model nonhydrostatic pressure effects [Mahadevan et al., 1996a,b, Marshall et al., 1997, Kanarska and Maderich, 2003, Kanarska et al., 2007, Wadzuk and Hodges, 2004]. Most of these models apply a pressure correction method to calculate the nonhydrostatic pressure and the related velocity corrections to correct the hydrostatic velocity field. Some of these correction methods are described in Armfield and Street [2002], Kanarska et al. [2007]. In the present study a two-dimensional form of a mode split $\sigma-$coordinate ocean model [Berntsen, 2004] with the capacity to include nonhydrostatic pressure effects is applied. The nonhydrostatic pressure correction methods used in the model are described in Berntsen and Furnes [2005], Keilegavlen and Berntsen [2009]. The model has earlier been used and tested in tank scale studies [Berntsen et al., 2006, 2008, Bergh and Berntsen, 2009].

The scale analysis made by Marshall et al. [1997] indicate that the hydrostatic approximation begin to break down somewhere between 1 and 10 km. This is only an indication of when nonhydrostatic pressure effects need to be accounted for. With increased resolution in the model, the influence of the nonhydrostatic pressure may continue to increase all the way down to grid resolution of a metre. With a resolution of about a metre, the vertical and horizontal length scales of motion will be of the same size. The dependency of the applied grid resolution on the strength and the influence of the nonhydrostatic pressure may depend strongly on the physical phenomena addressed. To study the influence of the nonhydrostatic pressure on a specific physical process, one may apply a simplified model. Gradually decreasing the horizontal grid size, the strength of the nonhydrostatic pressure is allowed to increase and the influence on the physical processes may be studied in a systematic manner. Running a hydrostatic and a nonhydrostatic model in a parallel set of calculations, the nonhydrostatic model results may also be compared to the corresponding hydrostatic results.

The wind and the tide, are the major sources of external energy into the ocean [Munk and Wunsch, 1998, Wunsch and Ferrari, 2004, Ferrari and Wunsch, 2009]. The tidal energy enter the ocean as a body force, acting in the whole water depth. The wind enter through the ocean surface and most of the wind forced energy is restricted to the surface layer, with only a minor part penetrating trough the pycnocline and reach the deeper layers in the ocean [Skyllingstad et al., 1999]. Together with the external energy sources, river discharges and rotational effects interact in the coastal ocean and create a complicated system [Huthnance, 1995, Davies and Xing, 2001, Xing and Davies, 2002, 2003]. To clarify the relation between these processes, it is common to simplify and only study some of the processes involved.

Wind forcing may advect water towards the coast, with the result of an increase in the water level. In a stratified ocean or lake, the circulation pattern and the barotropic pressure gradients at the coast will result in a baroclinic response in the form of downwelling. A simplified study by Kundu [1986] shows the combined effect of wind forcing and rotational effects in a two-dimensional model, with the coast in the form of a vertical wall. In another two-dimensional numerical model study, Austin and Lentz [2002] apply sloping lateral boundaries to study both upwelling and downwelling events. In a downwelling situation, the resulting displacement of the interface may create propagating internal waves [Heaps and Ramsbottom, 1966, Hall and Davies, 2005]. The development of the internal waves and the influence of nonhydrostatic pressure have been studied in an earlier work [Bergh and Berntsen, 2009]. In that study a simplified model was used, in the form of a two-dimensional closed basin of constant depth and without rotational effects. The amplitude and the form of the displacement of the interface will be important for the development of the propagating internal wave [Farmer, 1978, Horn et al., 2001]. With a shallow upper layer and a deeper lower layer, propagating internal waves of depression may undergo nonlinear steepening and take soliton forms. In the study by Bergh and Berntsen [2009], with the same forcing as in this work, a train of soliton waves developed after 60 h in a 400 km long basin. In that study, the horizontal resolution varied from 1 km down to 62.5 m, and with a horizontal resolution of $\Delta X = 125$ m, nonhydrostatic effects were strong enough in the steepening internal wave front to generate soliton waves. Though, even with a horizontal grid size of $\Delta X = 62.5$ m, the nonhydrostatic pressure effects were not strong enough during the first 20 h to influence the generation processes of the internal wave close to the boundary.

In the present study the model domain is reduced from 400 km down to 50 km, and an open boundary is introduced at the western side. Forcing values from a large scale model [Bergh and Berntsen, 2009] are applied in a 1 km long FRS-zone at the western open boundary. With a much smaller model domain, we are able to decrease the horizontal grid size further, to study possible nonhydrostatic pressure effects during the generation process of the internal wave.

2 Model

2.1 The governing equations

In the present study a two-dimensional version of a σ-coordinate ocean model is used. A detailed description of the used model can be found in Berntsen [2004]. This work can be described as a high resolution focused boundary layer study of the problem described in Bergh and Berntsen [2009]. In the coordinate system (x, z, t), where x is the horizontal coordinate, z the vertical coordinate, and t the time variable, the Reynolds averaged momentum equations using the Boussinesq approximation and assuming no rotational effects may be written

$$\frac{\partial U}{\partial t} + U\frac{\partial U}{\partial x} + W\frac{\partial U}{\partial z}$$

$$= -\frac{1}{\rho_0}\frac{\partial P}{\partial x} + \frac{\partial}{\partial x}(A_M\frac{\partial U}{\partial x}) + \frac{\partial}{\partial z}(K_M\frac{\partial U}{\partial z})\,, \tag{1}$$

$$\frac{\partial W}{\partial t} + U\frac{\partial W}{\partial x} + W\frac{\partial W}{\partial z}$$

$$= -\frac{1}{\rho_0}\frac{\partial P}{\partial z} - \frac{g\rho}{\rho_0} + \frac{\partial}{\partial x}(A_M\frac{\partial W}{\partial x}) + \frac{\partial}{\partial z}(K_M\frac{\partial W}{\partial z})\,. \tag{2}$$

The continuity equation for incompressible fluids is given by

$$\frac{\partial U}{\partial x} + \frac{\partial W}{\partial z} = 0\,. \tag{3}$$

In these calculations the conservation equation for density

$$\frac{\partial \rho}{\partial t} + U\frac{\partial \rho}{\partial x} + W\frac{\partial \rho}{\partial z} = \frac{\partial}{\partial z}(K_H\frac{\partial \rho}{\partial z}) + \frac{\partial}{\partial x}(A_H\frac{\partial \rho}{\partial x}) \tag{4}$$

is applied. In the equations above U and W are the horizontal and vertical velocity components respectively, P is the pressure, ρ is the density, g is the constant of gravity, and ρ_0 is the reference density.
The pressure P may be decomposed into pressure from the surface elevation η, internal pressure, and nonhydrostatic pressure P_{NH} according to

$$P(x,z,t) = g\rho_0\eta(x,t) + g\int_z^0 \rho(x,\acute{z},t)d\acute{z} + P_{nh}(x,z,t), \tag{5}$$

where the calculation of P_{nh} is described in Section 2.2. To formulate a uniform approach for the subgrid scale closure with a varying horizontal grid size, we apply a two dimensional form of the Smagorinsky formulation to calculate the horizontal viscosity A_M. The eddy viscosity parameter, in the Smagorinsky formulation, is set to $C_M = 5.0$ in calculations 1 to 3, with $\Delta X = 100,\ 50,$ and $25\,\mathrm{m}$, and to $C_M = 10.0$ in calculation 4, with $\Delta X = 12.5\,\mathrm{m}$. The vertical viscosity is set to a constant value, $K_M = 4.0\times10^{-3}\,\mathrm{m^2\,s^{-1}}$ together with constant low values of the horizontal and vertical diffusivity, $A_H = K_H = 1.0\times10^{-6}\,\mathrm{m^2\,s^{-1}}$. When the model is used in the hydrostatic mode, the vertical momentum equation, Eq. (2), is replaced by

$$\frac{\partial P}{\partial z} = -\rho g\,, \tag{6}$$

which describes the hydrostatic balance, and only the hydrostatic part, P_H, of the pressure is used, the two first terms on the right hand side of Eq. (5).

The equations described above in the (x,z,t) coordinate system are transformed into a σ-coordinate system (x^*,σ,t^*) in the numerical model, see Berntsen [2004].

The variables are discretised on a C-grid. In these calculations a Total Variance Diminishing (TVD) advection scheme with a superbee limiter is applied. The time stepping is performed with a predictor-corrector method. The leapfrog method is used as the predictor and the fully implicit method is used as the corrector. Mode splitting is applied and the velocity field is divided into a depth averaged part, with the time step $\overline{\Delta}t = \Delta t/30$ and a deviation from the depth averaged part, with the time step Δt. The resolution in time is adjusted according to the horizontal resolution to avoid numerical instabilities and is described in Table 1.

2.2 Nonhydrostatic pressure

The pressure is split into a hydrostatic part, P_h, and a nonhydrostatic part, P_{nh}. The hydrostatic version of the governing equations are used to calculate a provisional velocity field. Subsequently the convergence and divergence in the provisional velocity field are used to calculate P_{nh}. Correction velocities may then be calculated due to the gradients in the nonhydrostatic pressure field, with the result of a divergence free velocity field. Similar methods are used as in Casulli [1990], Marshall et al. [1997], Kanarska and Maderich [2003], Kanarska et al. [2007] and were first introduced in the present model by Heggelund et al. [2004]. Heggelund et al. used a similar method as in Kanarska and Maderich [2003] and transformed the correction methods onto the $\sigma-$coordinate system. The $\sigma-$transformation complicate the calculations, and it was suggested in Berntsen and Furnes [2005] to solve the nonhydrostatic pressure directly in the $\sigma-$coordinate system, $P_{nh}(x, y, \sigma)$. The approach introduced by Berntsen and Furnes [2005] is used in the present model and will simplify the calculation. The methods used in the present work are compared to the transformation method used in Kanarska and Maderich [2003] by Keilegavlen and Berntsen [2009]. It is shown that similar pressure and velocity fields are produced with the two different methods [Keilegavlen and Berntsen, 2009].

2.3 Numerical calculations

The model is closed at the eastern coast, where no volume fluxes and a free slip condition is applied. An open boundary is applied at the western coast. The basin length $L = 50\,\mathrm{km}$ and the constant depth $H = 250\,\mathrm{m}$. The calculations are initialised with two separate layers, each with a separate constant density gradient $\partial\rho/\partial z$. In the $100\,\mathrm{m}$ deep upper layer $\partial\rho/\partial z = 0.02\,\mathrm{kg\,m^{-4}}$ and in the $150\,\mathrm{m}$ deep lower layer $\partial\rho/\partial z = 0.001\,\mathrm{kg\,m^{-4}}$.

The model is forced at the surface with a sinus formed wind pulse over $T_W = 12\,\mathrm{h}$, with the maximum wind stress $\tau_{max} = 0.5\,\mathrm{N\,m^{-2}}$. The wind stress τ_s, will then be

$$\tau_s = \begin{cases} \tau_{max} \sin\left(\frac{\pi t}{T_W}\right) & \text{for} \quad 0 \le t \le T_W\,, \\ 0 & \text{for} \quad t > T_W\,. \end{cases} \tag{7}$$

The effects of the wind stress and the bottom friction are calculated with a drag coefficient method. The model run over $T = 20\,\mathrm{h}$. In this study 126 equidistant vertical $\sigma-$layers are used, implying a vertical resolution of $2\,\mathrm{m}$. The horizontal resolutions, ΔX, are given in Table 1.

Table 1: Summary of the numerical calculations, horizontal grid points IM, horizontal resolution $\Delta x\,(m)$, the time step in the model, $\Delta t\,(s)$, and numbers of cells in the FRS-zone, LB, in both a hydrostatic, a), and a nonhydrostatic, b), mode

Case	IM	ΔX	Δt	LB
1 a,b	511	100	4	10
2 a,b	1021	50	2	20
3 a,b	2041	25	1	40
4 a,b	4081	12.5	0.5	80

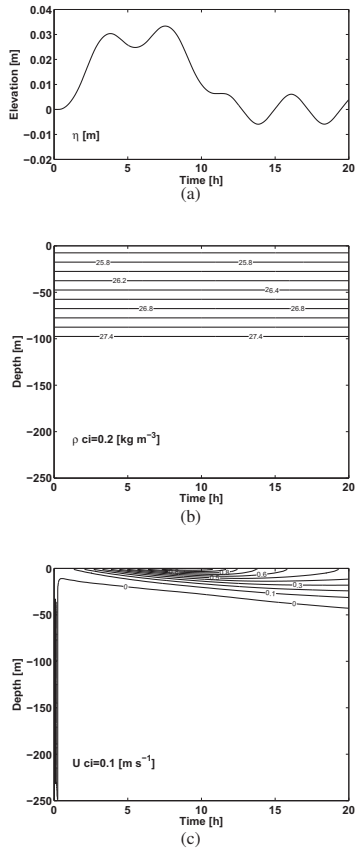

Figure 1: Forcing reference values in the FRS-zone, a) the surface amplitude, η (m), b) the density stratification, ρ (kg m^{-3}), and c) the horizontal velocity, U (m s^{-1}).

At the open boundary, variables are relaxed towards reference levels taken from a large scale model. This is done in a 1 km long open boundary using a flow relaxation zone (FRS-zone) application [Martinsen and Engedahl, 1987]. The number of cells in the FRS-zone, LB, will be different with different horizontal resolution and is described in Table 1. The variable ϕ are adjusted in the FRS-zone at each time step according to

$$\phi \quad = \quad (1-\alpha)\phi_{int} + \alpha\phi_{ref}\,,$$

where ϕ_{int} is the un-relaxed values computed by the model and ϕ_{ref} is a specified reference value. The relaxation parameter α varies from 1 at the first grid cell at the western side of the computational domain to 0 at the end of the FRS-zone facing the interior model domain. The reference values ϕ_{ref} are taken from a model with a closed 400 km long

basin and with the same wind forcing described in this work, see Bergh and Berntsen [2009] for a more detailed description. The reference calculation is done with a horizontal resolution of $\Delta X = 1\,\text{km}$ and a vertical resolution of 126 σ-layers. The values from the reference calculation are taken at the same position as the position of the FRS-zone in this work, at a distance of $50\,\text{km}$ from the eastern coast. The relaxed variables are the surface elevation, $\eta(t)$, the density profile, $\rho(z,t)$, the depth averaged horizontal velocity, $\overline{U}(t)$, and the horizontal velocity profile, $U(t,z)$. The reference values for these variables are presented in Fig. 1. The variables are linearly interpolated in time to fit with the resolutions in the different calculations. The relaxed variables in the FRS-zone at the western boundary will then be forced towards the values extracted from the large scale model.

3 Results

The wind pulse generates a wind forced surface layer that advect water towards the eastern coast. This will set up the surface at the coast and generate a barotropic pressure gradient directed away from the coast. Downwelling at the coast push down lighter water masses and an internal baroclinic pressure gradient will partly balance the barotropic counterpart, in the stratified water mass. The wind forced advection in the surface, together with the total pressure gradient, generate a circulation pattern in the form of a wind forced surface layer, downwelling close to the coast and a weak return flow below the surface layer, see Figs. 2, 3, and 4. The downwelling at the coast generates an internal wave of depression that propagates away from the coast. This internal wave of depression may later (not presented in this work) undergo nonlinear steepening and develop into a soliton wave form Horn et al. [2001], Farmer [1978], Bergh and Berntsen [2009].

There are significant differences between the results with a horizontal resolution of $\Delta X \geq 25\,\text{m}$ and the results with $\Delta X = 12.5\,\text{m}$, and the results are presented in two different sections accordingly.

3.1 Results for $\Delta X = 100,\, 50,$ and $25\,\text{m}$

The wind forcing has a period of $12\,\text{h}$, starting from zero and increasing to a maximum at $6\,\text{h}$, and decreasing to zero at $12\,\text{h}$ and after, see Section 2.3. The advection in the wind forced surface layer continues to increase after the maximum in the wind pulse, and reach a maximum in the horizontal velocity component around $10\,\text{h}$. The strength of the advection starts to decrease after $10\,\text{h}$, even though the advective surface layer continues to deepen during all the modelled period. With the same vertical viscosity in these calculations, the development of the wind forced surface layer may be described by the forcing horizontal velocities in the FRS-zone, see Fig. 1. The vertical extent of the advective surface layer reach to a depth of about $20\,\text{m}$ at $10\,\text{h}$, and to about $40\,\text{m}$ at $20\,\text{h}$. The advection of water towards the east coast increase the water elevation at the coast. The elevation reach a maximum at the same time as the maximum in advection occur, around $10\,\text{h}$.

Both the advection and the variation of the water elevation are strongly dependent on the forcing at the open boundary, see Fig. 1. From the forcing surface elevation in the FRS-zone, one may detect two clear signals. First, the $12\,\text{h}$ period signal from the forcing wind pulse and, on top of that, a signal with shorter period. The signal with shorter period is connected to the period of a surface standing wave in the large scale model, from where the forcing surface elevation is taken. The period of a surface standing wave in a closed basin may be calculated to $T(n) = (2\,L/(n\,c))$ for wave mode n, where L is the length

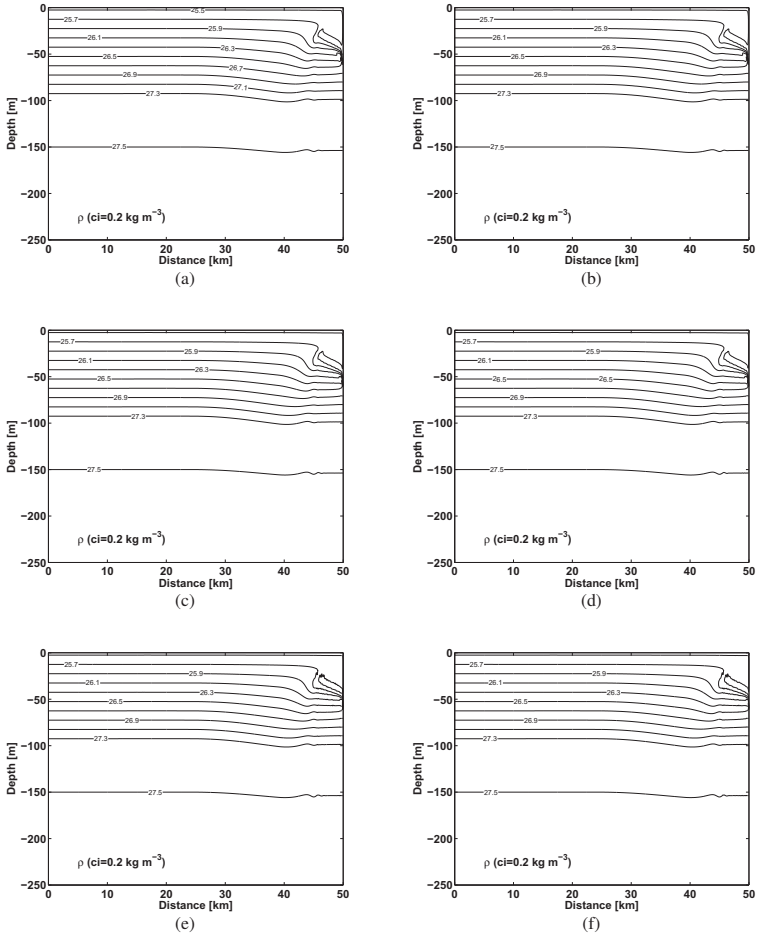

Figure 2: Density stratification, ρ ci=0.2 kg m^{-3}, at 10 h with the nonhydrostatic calculation to the left (a, c, e) and hydrostatic calculation to the right (b, d, f) and with the horizontal grid sizes $\Delta X = 100$ m (a, b), $\Delta X = 50$ m (c, d), and $\Delta X = 25$ m (e, f)

of the closed basin, $c = (g\,H)^{-1/2}$ is the speed of a surface gravity wave with the gravity constant g and the water depth H. With a basin length $L = 400$ km and depth $H = 250$ m, in the large scale model, the first mode ($n = 1$) surface standing wave period is calculated to $T = 4.5$ h. This period is in agreement with the short period signal seen in the forcing surface elevation in Fig. 1.

The advection of water towards the coast results in a zone of downwelling close to the

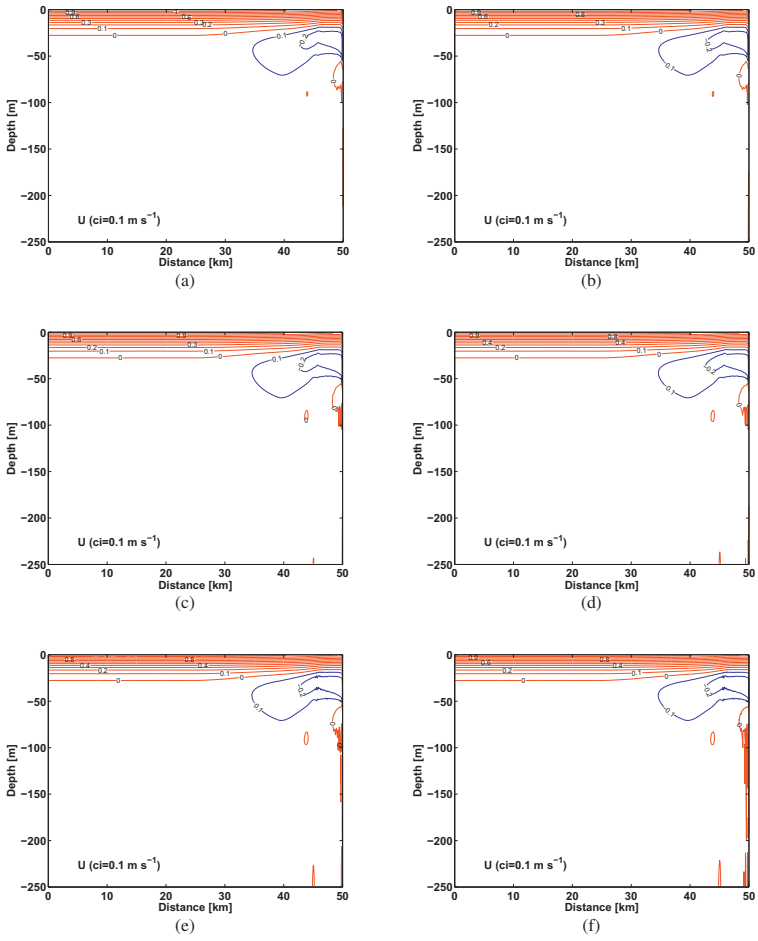

Figure 3: Horizontal velocity, u ci=0.1 m s^{-1}, at 10 h with the nonhydrostatic calculation to the left (a, c, e) and hydrostatic calculation to the right (b, d, f) and with the horizontal grid sizes $\Delta X = 100$ m (a, b), $\Delta X = 50$ m (c, d), and $\Delta X = 25$ m (e, f)

boundary, see Fig. 5. Light surface water is pushed down at the boundary, to a depth of approximately 50 m, see Fig. 4. The downwelling is strong enough to create overturning and convective mixing in the upper 50 m, see Fig. 2. The downwelling flow separate from the boundary and form a return flow, below the wind forced surface layer, transporting water away from the east coast , see Fig. 3. The strong downwelling at the boundary create a sharp density interface around 50 m depth, see Fig. 6.

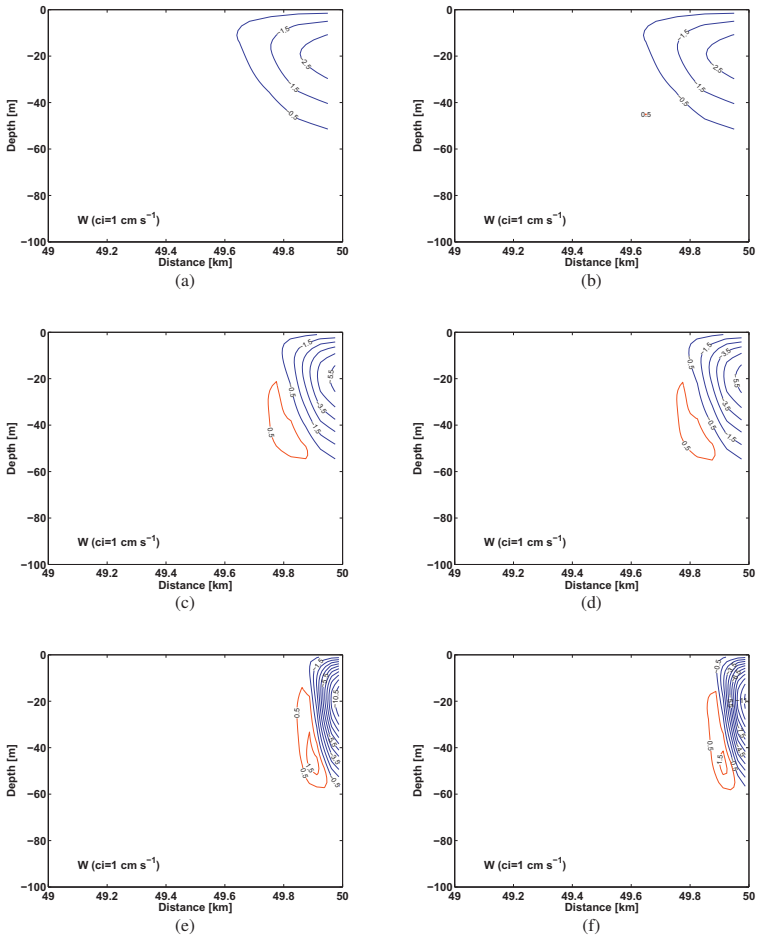

Figure 4: Focus over boundary layer, 49 to 50 km, vertical velocity, w ci=1 cm s^{-1}, at 10 h with the nonhydrostatic calculation to the left (a, c, e) and hydrostatic calculation to the right (b, d, f) and with the horizontal grid sizes $\Delta X = 100$ m (a, b), $\Delta X = 50$ m (c, d), and $\Delta X = 25$ m (e, f)

The density stratification in Fig. 2 indicate that all the calculations 1 to 3, both hydrostatic and nonhydrostatic, give similar results at 10 h. At this stage, the depression wave, propagating away from the boundary, has a more gentle slope in the front and a more abrupt change in the rear end.

With a horizontal resolution of $\Delta X = 100$ m, the negative vertical velocities in connec-

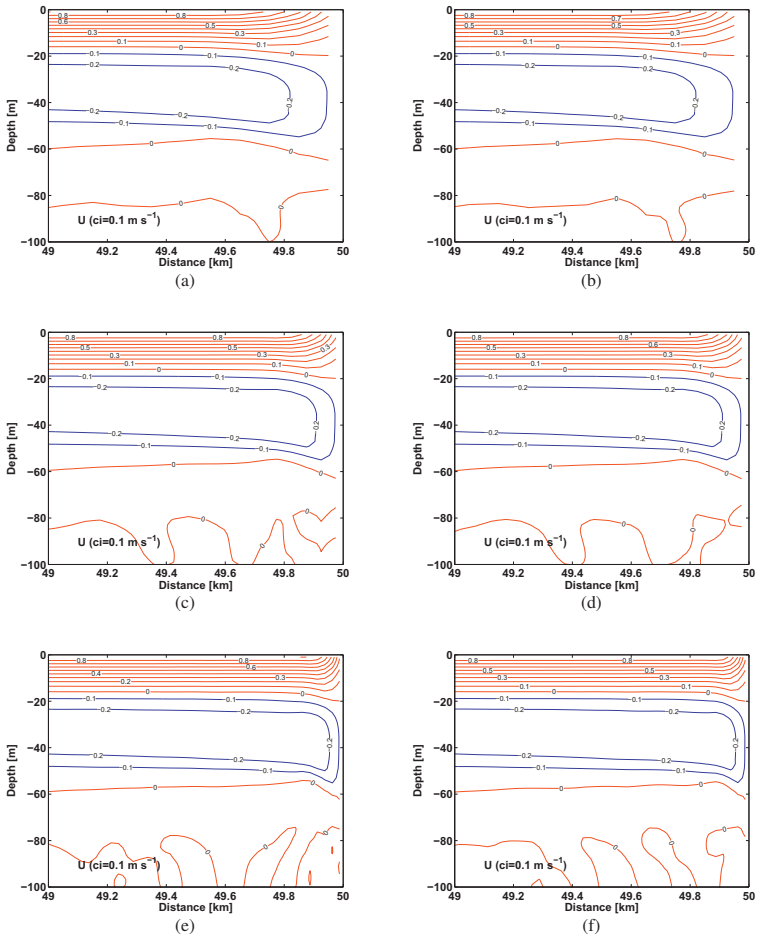

Figure 5: Focus over boundary layer, 49 to $50\,\mathrm{km}$, horizontal velocity, u ci=0.1 $\mathrm{m\,s^{-1}}$, at $10\,\mathrm{h}$ with the nonhydrostatic calculation to the left (a, c, e) and hydrostatic calculation to the right (b, d, f) and with the horizontal grid sizes $\Delta X = 100\,\mathrm{m}$ (a, b), $\Delta X = 50\,\mathrm{m}$ (c, d), and $\Delta X = 25\,\mathrm{m}$ (e, f)

tion with the downwelling at the boundary layer reach a maximum amplitude of $-2.5\,\mathrm{cm\,s^{-1}}$, see Fig. 4. The downwelling reach down to a separation point at approximately $50\,\mathrm{m}$ depth. With increased horizontal resolution, the negative vertical velocity in the boundary layer increase further in magnitude. When the horizontal grid size is halved, the size of the negative velocity amplitude is doubled in the results with $\Delta X = 50\,\mathrm{m}$ and $\Delta X = 25\,\mathrm{m}$, see

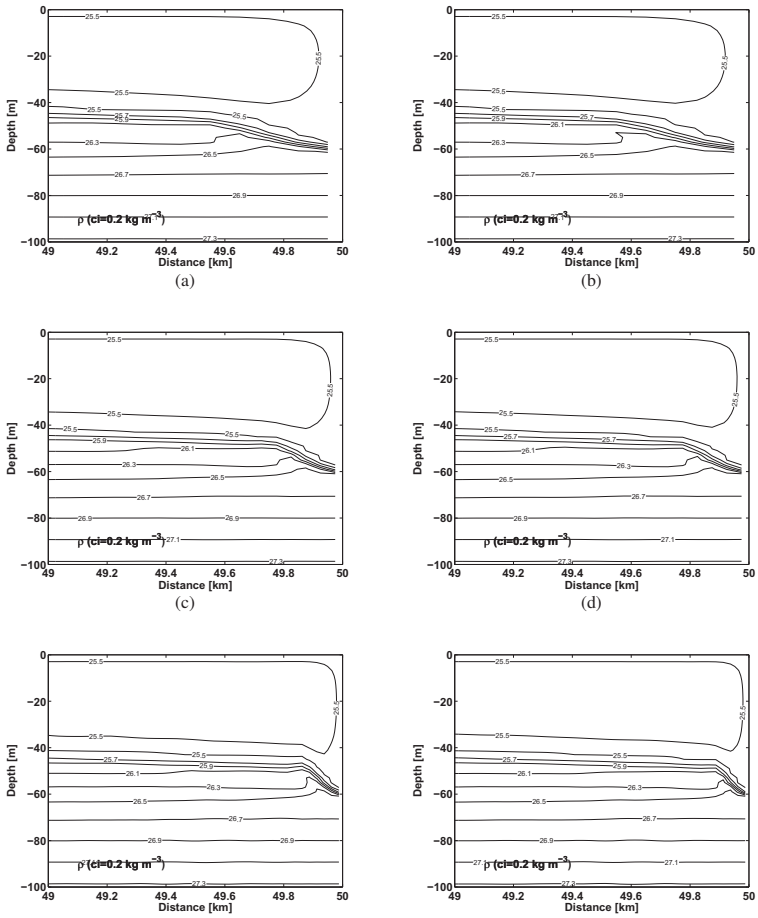

Figure 6: Focus over boundary layer, 49 to 50 km, density stratification, ρ ci=0.2 kg m^{-3}, at 10 h with the nonhydrostatic calculation to the left (a, c, e) and hydrostatic calculation to the right (b, d, f) and with the horizontal grid sizes $\Delta X = 100$ m (a, b), $\Delta X = 50$ m (c, d), and $\Delta X = 25$ m (e, f)

Fig. 4. In the results with $\Delta X = 50$ m the intensification of the downwelling zone result in a upward directed flow, just outside the downwelling zone, see Fig. 4 c) and d). The vertical velocities in the upward directed flow, further increase in the results with $\Delta X = 25$ m, see Fig. 4 e) and f).

The calculated maximum and minimum vertical velocities in the whole domain, are

found in the boundary layer, and are presented in Fig. 7. The maximum and minimum velocities following the same pattern as the horizontal advection in the surface, with maximum amplitudes found around 10 h. Also the horizontal extent of the downwelling zone is reduced with decreased horizontal grid size. The horizontal extent decrease from approximately 400 m, to 200 m, and to 100 m when the horizontal grid size is reduced from 100 m, to 50 m, and to 25 m respectively. This gives a horizontal extent of the downwelling zone of approximately 4 grid cells in all calculations, see Fig. 4.

Studying the interface displacement in Fig. 8, we can conclude that the increased velocities, together with the reduced horizontal extent of the downwelling zone, result in a relatively constant vertical volume flux in the boundary layer. The increased vertical velocities result in an area with intensified convergence in the boundary layer and increased values of the nonhydrostatic pressure, see Fig. 9. Even so, the nonhydrostatic pressure does not affect the general density stratification or the circulation pattern in the results with $\Delta X \geq 25$ m.

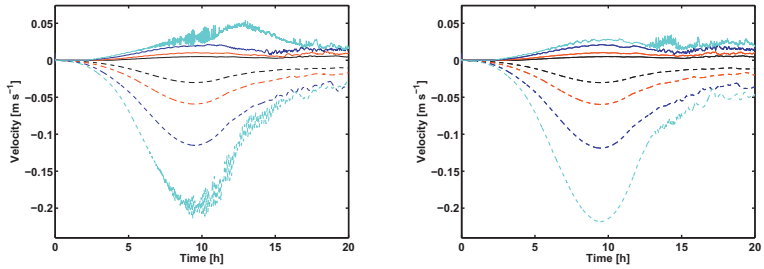

Figure 7: Maximum (line) and minimum (dotted line) vertical velocity ($\mathrm{m\,s^{-1}}$) in a) the nonhydrostatic calculations respectively b) the hydrostatic calculations, with the horizontal grid size $\Delta X = 100$ m (black), $\Delta X = 50$ m (red), $\Delta X = 25$ m (blue), $\Delta X = 12.5$ m (light blue)

At 20 h the internal wave of depression has propagated further away from the east coast. The front of the wave has almost reached the open boundary at the western side, and the sharp rear end of the wave is found at a distance of approximately 35 km from the west coast, see Fig. 8. The well mixed zone in the upper 50 m continues to expand horizontally, following the propagating internal wave, see Fig. 10. At this time, instabilities have been generated at the eastern boundary, and the instabilities become stronger with reduced horizontal grid size. Studying the maximum and minimum vertical velocities in Fig. 7, one may deduce that there are stronger variability after 15 h in the results with $\Delta X = 25$ m, indicating that the instabilities start at this time. The results also show that the instabilities begin later in the calculation with larger horizontal grid sizes, $\Delta X = 100$ m and $\Delta X = 50$ m. Though, in the results with $\Delta X \geq 25$ m, the instabilities are limited to an area behind the propagating internal wave, and have not spread further away than approximately 15 km away from the east coast at 20 h, see Fig. 8.

One may expect instabilities and mixing to take place in the rear end of the wave. The density gradients are compressed in the rear end of the wave, and this may create an area

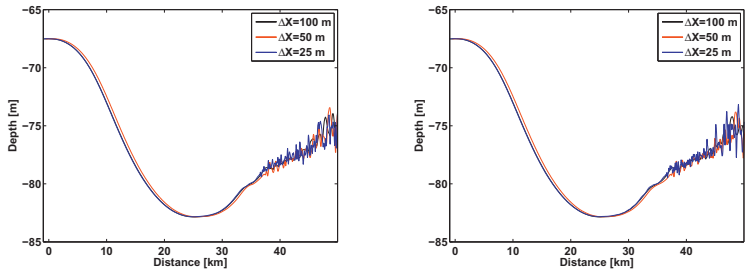

Figure 8: Interface displacement, $\rho_{int} = 1026.8\,\mathrm{kg\,m^{-3}}$, in a) nonhydrostatic respectively b) hydrostatic calculations, with the horizontal grid size $\Delta X = 100\,\mathrm{m}$ (black), $\Delta X = 50\,\mathrm{m}$ (red), and $\Delta X = 25\,\mathrm{m}$ (blue)

with low Richardsson numbers. This is often seen in propagating solitary waves in the ocean where Kelvin-Helmholtz (KH) instabilities may grow in this area, see for instance Moum et al. [2003]. There are few similar numerical calculations as the present, with a wind induced initial depression. In numerical experiments it is common to initialise the model with a depression at the boundary in the form of half soliton wave with a double amplitude Bourgault and Kelley [2003], Thiem and Berntsen [2009]. If there are no shear instabilities, this type of initialisation give a smooth transition to a propagating single soliton without instabilities. In laboratory experiments it is common to initiate the wave propagation by removing a gate that separates two water masses of different vertical stratification [Michallet and Ivey, 1999, Grue et al., 1999]. In these experiments some instabilities and mixing will take place during the generation phase of the wave. Shear instabilities are clearly seen in both the generation phase and in the rear end of the propagating internal wave in unpublished numerical calculations by Barad and Fringer [2009].

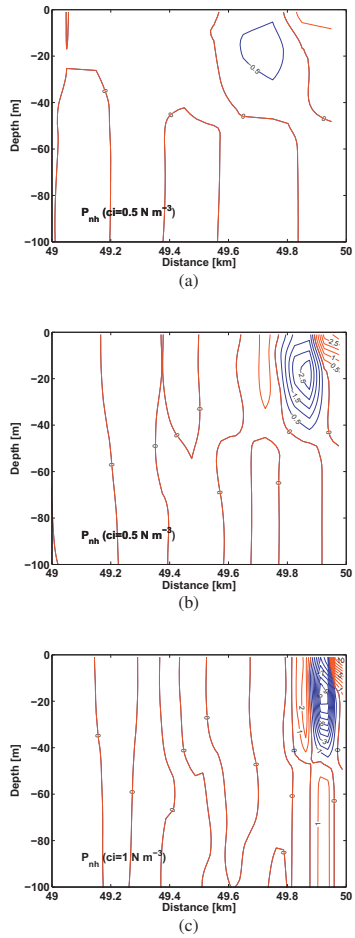

Figure 9: The nonhydrostatic pressure P_{nh} ($\mathrm{N\,m^{-2}}$) at 10 h over the boundary layer from 49 to 50 km. Results produced with $\Delta X = 100$ m are given in a), with $\Delta X = 50$ m in b), and $\Delta X = 25$ m in c). Notice the change in the contour interval, ci, in panel c)

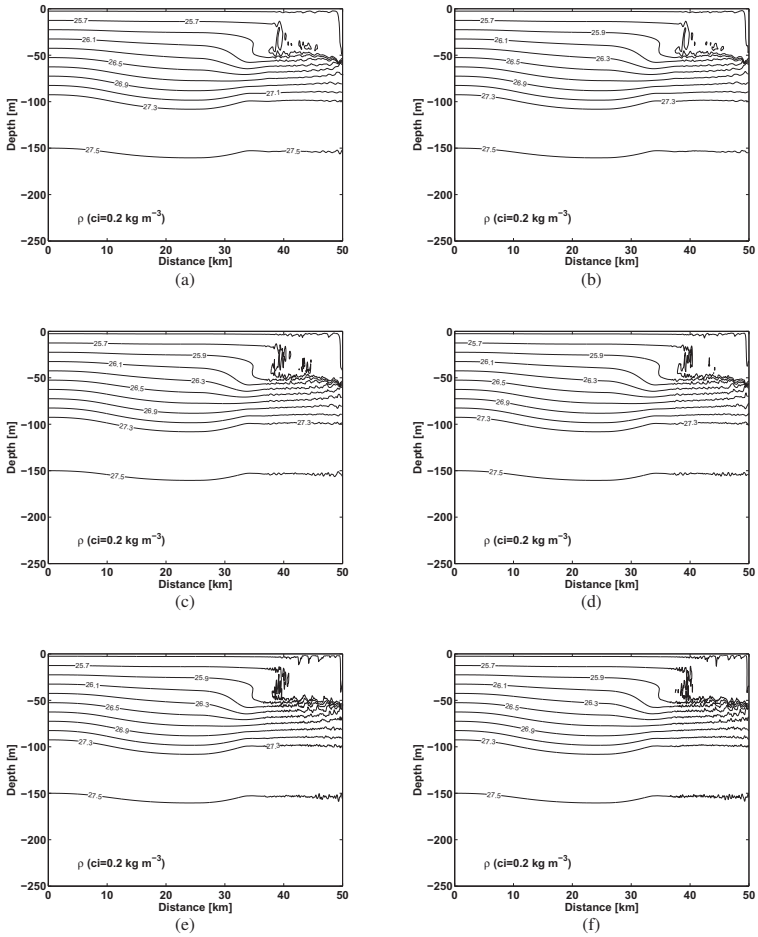

Figure 10: Density stratification, ρ ci=0.2 kg m^{-3}, at 20 h with the nonhydrostatic calculation to the left (a, c, e) and hydrostatic calculation to the right (b, d, f) and with the horizontal grid sizes $\Delta X = 100$ m (a, b), $\Delta X = 50$ m (c, d), and $\Delta X = 25$ m (e, f)

3.2 Results with $\Delta X = 12.5\,\mathrm{m}$

When the horizontal grid size is reduced to 12.5 m, the horizontal extent of the downwelling zone at the eastern coast is further reduced and the amplitude of the vertical velocity is further increased at 10 h, see Figs. 11 and 12. The horizontal extent of the downwelling zone is almost halved, compared to calculations with $\Delta X = 25$ m, and extend about 60 to 70 m from the east coast, see Figs. 11 e) and 12 e). The negative vertical velocity increase to a maximum amplitude of $-19\,\mathrm{cm\,s^{-1}}$ close to the boundary. With increased vertical velocities at the boundary, the density stratification below the separation point, around 50 m depth, is further compressed, see Figs. 11 c) and 12 c).

To indicate the overall influence of the nonhydrostatic pressure, the norms of the horizontal hydrostatic pressure gradients and the horizontal nonhydrostatic pressure gradients are calculated during the modelled period, see Fig. 13. The development in time show that the nonhydrostatic norm grow much faster than the hydrostatic norm during the first 10 h. There is a periodic variation of the hydrostatic norm with $\Delta X = 12.5$ m, and the nonhydrostatic norm may be stronger than the hydrostatic counter part. The period of the hydrostatic norms is similar to the one found in the forcing surface amplitude, see Fig. 1, and may be related to this. Also the time mean value of the nonhydrostatic norm grow to the same order of magnitude as the hydrostatic counterpart with a grid resolution of 12.5 m, though still half of the hydrostatic value, see Fig. 14.

The pressure gradients in the fluid drive the flow, and with nonhydrostatic pressure gradients of the same size as the hydrostatic pressure gradients, one can expect that the nonhydrostatic pressure effects will influence the flow in the model. With a horizontal resolution of 12.5 m, the nonhydrostatic pressure becomes strong enough to affect both the density and the velocity fields, see Figs. 11 and 12. With increased resolution the model is able to contain more energy on smaller scales. Even so, the resolution may not be high enough to resolve the physical processes involved in the generation processes of the wave, and the strong forcing in the system may result in unphysical large instabilities. A clear difference is now seen between the hydrostatic and the nonhydrostatic results. The variation in the velocity field generate a strong and fluctuating nonhydrostatic pressure field, see Fig. 11.

The instabilities generated in the rear end of the wave, close to the boundary, are transported further into the model domain in the nonhydrostatic results. One may think that the nonhydrostatic pressure, counteracting vertical velocities, may damp the variations in the velocity field and that more mixing will take place in the hydrostatic model. The contrary is seen in the results presented here. The nonhydrostatic pressure act as a mechanism to transport the instabilities into the model domain, and a larger area may be exposed to mixing, compare Fig. 11 a) and c) to Fig. 12 a) and c). This may also be deduced from the results at 20 h, see Fig. 15.

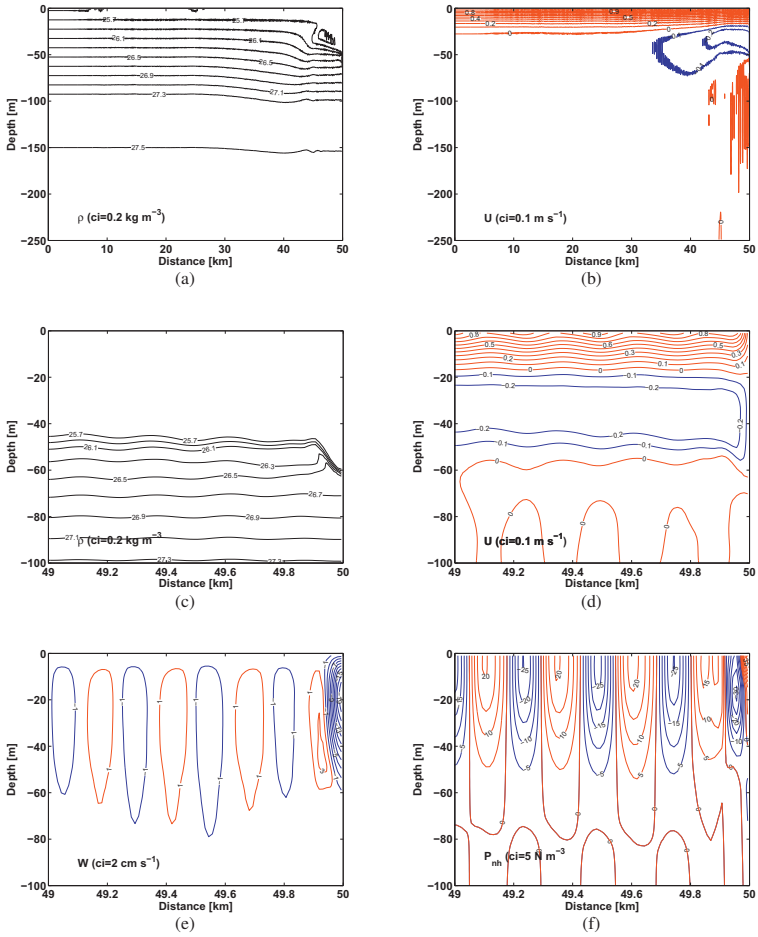

Figure 11: Results from the nonhydrostatic calculation at 10 h with $\Delta X = 12.5$ m. a) density stratification, ρ ci=0.2 kg m^{-3}, b) horizontal velocity, u ci=0.1 m s^{-1}, c) vertical velocity, w ci=1 cm s^{-1}, and d) nonhydrostatic pressure, P_{nh} ci=5 N m^{-2}

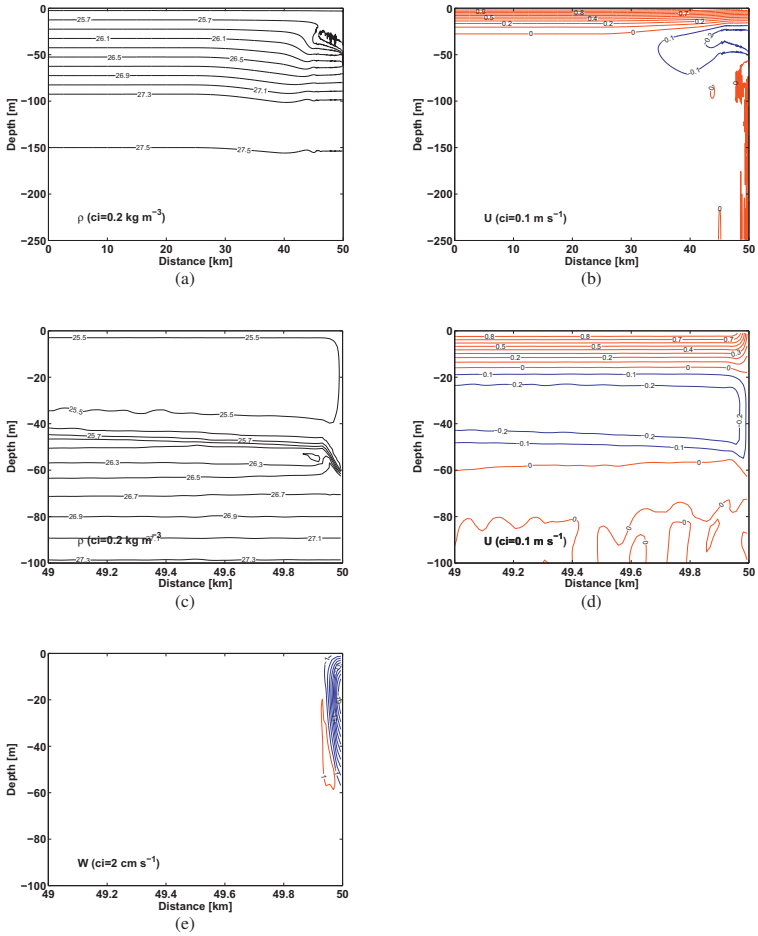

Figure 12: Results from the hydrostatic calculation at 10 h with $\Delta X = 12.5$ m. a) density stratification, ρ ci=0.2 kg m^{-3}, b) horizontal velocity, u ci=0.1 m s^{-1}, and c) vertical velocity, w ci=1 cm s^{-1}

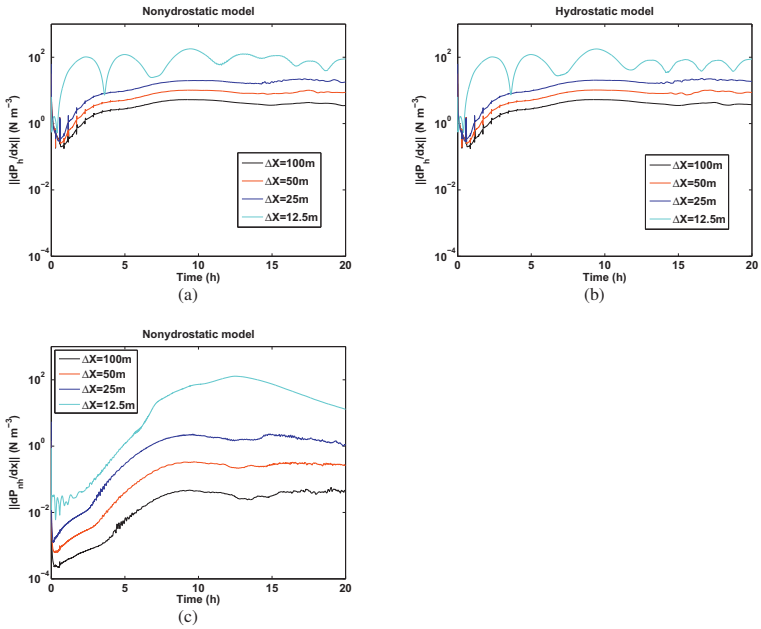

Figure 13: The norm of the horizontal hydrostatic pressure gradient in a) the nonhydrostatic calculations and b) the hydrostatic calculations and c) the norm of the horizontal nonhydrostatic pressure gradient in the nonhydrostatic calculations, with the horizontal grid size $\Delta X = 100\,\mathrm{m}$, $\Delta X = 50\,\mathrm{m}$, $\Delta X = 25\,\mathrm{m}$, and $\Delta X = 12.5\,\mathrm{m}$

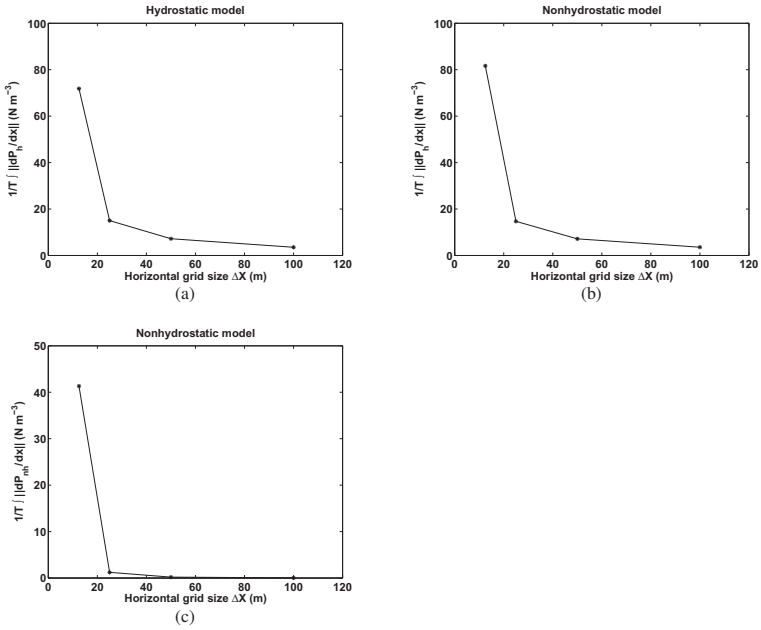

Figure 14: The mean norm of the horizontal hydrostatic pressure gradient in a) the hydrostatic calculations and b) the nonhydrostatic calculations and c) the mean norm of the horizontal nonhydrostatic pressure gradient in the nonhydrostatic calculations, with the horizontal grid size $\Delta X = 100\,\mathrm{m}$, $\Delta X = 50\,\mathrm{m}$, $\Delta X = 25\,\mathrm{m}$, and $\Delta X = 12.5\,\mathrm{m}$

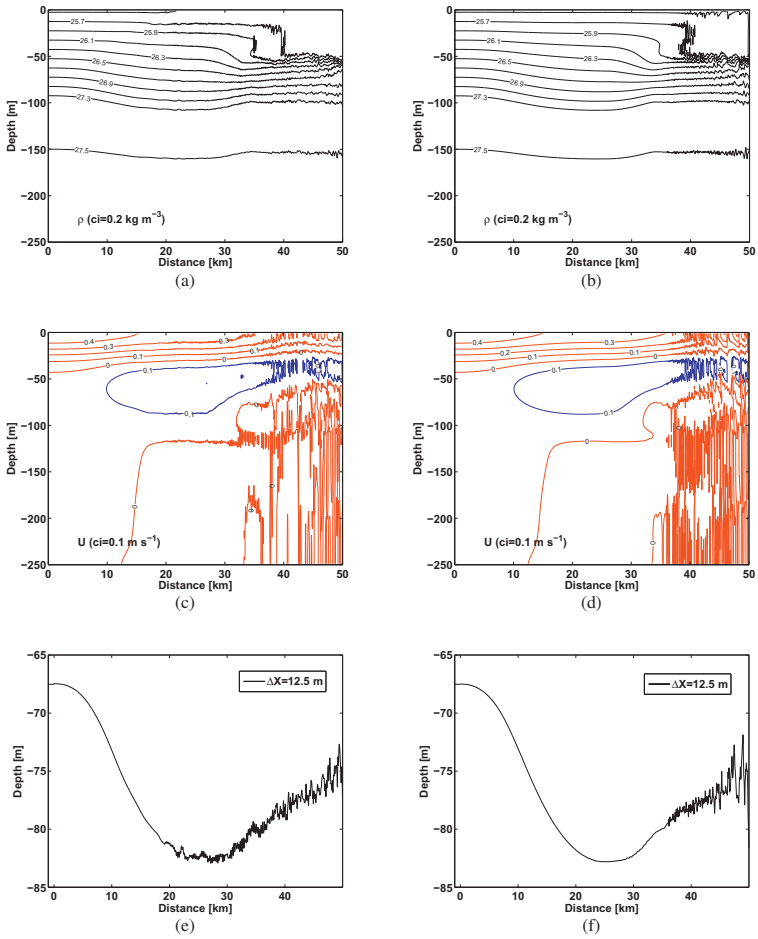

Figure 15: Results from the calculations with $\Delta X = 12.5\,\mathrm{m}$ at 20 h. Nonhydrostatic results to the left and hydrostatic results to the right. a) and b) density stratification, ρ ci=0.2 kg m^{-3}, and c) and d) horizontal velocity, U ci=0.1 m s^{-1}, and e) and f) the interface displacement of $\rho_{int} = 1026.8\,\mathrm{kg\,m^{-3}}$

4 Discussion

In the present work we study the generation of wind induced internal waves. In a study with a similar forcing as in the present work, using a grid resolution of $62.5\,\mathrm{m}$, the nonhydrostatic pressure effects were too small during the generation phase to influence the wave. With a higher resolution one may expect that the nonhydrostatic pressure effects become stronger. Introducing an open boundary (FRS-zone) at the western side in the present work, the model domain is reduced and we are able to study the influence of nonhydrostatic pressure during the generation phase with a higher resolution.

The strong forcing in the FRS-zone together with the constant value of the vertical eddy viscosity in all calculations, result in relatively robust fluxes in and out of the FRS-zone. Even if the horizontal extent of the downwelling zone decrease when the grid size is reduced, the vertical velocities increase with the same rate and the vertical volume flux in the downwelling zone is relatively constant. The amplitude and the length scale of the generated internal waves are very similar in all calculations. The nonhydrostatic pressure field becomes stronger every time the grid size is further decreased, with the present range of grid scales. Though, there are no visible nonhydrostatic pressure effects with $\Delta X \geq 25\,\mathrm{m}$. When the grid size is reduced to $\Delta X = 12.5\,\mathrm{m}$, the nonhydrostatic pressure effects become strong enough to influence both the velocity and the density fields. The instabilities generated at the rear end of the wave are growing stronger when the grid size is reduced. The instabilities are restricted to a focused area close to the boundary in all calculations with $\Delta X \geq 25\,\mathrm{m}$. In the nonhydrostatic calculation with $\Delta X = 12.5\,\mathrm{m}$, the instabilities and the correlated mixing are transported away from the boundary and are visible in a larger part of the model domain at $20\,\mathrm{h}$. This is not seen in the hydrostatic results where the instabilities and the mixing are restricted to an area closer to the boundary.

With $\Delta X = 12.5\,\mathrm{m}$ the model is not able to fully resolve the small scale physical processes. With higher resolution one may expect that the physical processes on smaller scale will be better represented. In the present calculations, the energy cascade towards the grid scale does not result in any "real" physical process on smaller scales, and the only way to balance for this energy cascade would be to increase the parametrised mixing in the model. When the horizontal grid size is reduced in a numerical model one may enter into a new type of "regime". This is well known for larger domain three dimensional ocean models that go from a regime where horizontal eddies are not represented, through a eddy permitting regime, and finally into a eddy resolving regime as the grid size is reduced. With the present range of grid sizes we go from a regime where the nonhydrostatic pressure effects are very small and into a regime that permit nonhydrostatic adjustments of the flow fields and associated instabilities, without fully resolving the physical processes in that regime. With higher resolution we may be able to resolve the physical processes involved.

At interfaces similar to the one found in the present experiments there may be Kelvin-Helmholtz instabilities, see Kundu [1990]. For idealised cases, it may be shown that waves shorter than a given criteria are unstable. Using such a criteria, from Kundu [1990], we have estimated the critical length scale for our set of parameters to be approximately $2\,\mathrm{m}$. This means that these unstable modes may not be resolved with the grid sizes used in our experiments. Even so, there may be a flow of energy towards the length scale associated with Kelvin-Helmholtz instabilities that creates the wave like pattern found in our results for $\Delta X = 12.5\,\mathrm{m}$. This transformation into a nonhydrostatic permitting and into a nonhydrostatic resolving regime for the case of tidal flow over a sill is recently discussed in Berntsen et al. [2009].

To be able to perform a study where the horizontal grid size is gradually decreased,

both the vertical and the horizontal subgrid scale parametrisation have to be treated carefully. With increased resolution, the energy spectra is broadened and the models capacity to contain more energy at smaller scales should be increased. There are several problems connected to the model set up in the present experiments. These may be divided into three parts, (1) the open boundary, (2) the strong vertical downwelling at the boundary, and (3) the variation in the horizontal grid resolution. All these problems are related to each other and to the choice of the subgrid scale parametrisation. The open boundary condition should simulate the motions and forcing in the large scale model. To prohibit imbalance in the horizontal fluxes between the FRS-zone and the interior of the model, the vertical mixing has to be treated in a similar way in the FRS-zone as in the interior of the model. Accordingly, the same constant values of vertical eddy viscosity and diffusivity are chosen in the calculation of the forcing values to be used in the FRS-zone and in all the calculations in the present experiments. With increased horizontal resolution, one may not only expect differences in the horizontal but also in the vertical, and this may be problematic when the vertical viscosities and diffusivities are kept constant.

When the horizontal grid size is reduced, the horizontal extent of the downwelling zone at the east coast is reduced and the amplitude of the negative vertical velocity is increased. This focusing of the downwelling zone create higher values of horizontal gradients in the vertical velocity field and increased shear strain. In the present experiments, with moderate values of viscosity, the flow of energy towards smaller grid scales create waves with a length scale of approximately $10 - 20$ times the grid size. These are the shortest waves that may be represented by models based on first and second order approximations. In reality, the energy will be transported to even smaller scales, and in future experiments with grid sizes of approximately 1 m Kelvin-Helmoltz type instabilities may be represented.

Acknowledgement

This research has received support from The Research Council of Norway through the MARE programme grant 164501/S40.

References

S. Armfield and R. Street. An analysis and comparison of the time accuracy of fractional-step methods for the Navier-Stokes equations on staggered grids. *Int. J. Numer. Methods Fluids*, 38:255–282, 2002. 1

J.A. Austin and S.J. Lentz. The inner shelf response to wind-driven uppwelling and downwelling. *Journal od Physical Oceanography*, 32:2171–2193, 2002. 1

M.F. Barad and O.B. Fringer. Simulations of shear instabilities in interfacial gravity waves. Under consideration for publication for J Fluid Mech, 2009. http://www.stanford.edu/ barad/movies.html. 3.1

J. Bergh and J. Berntsen. Numerical studies of wind forced internal waves with a nonhydrostatic model. *Ocean Dyn*, 2009. doi:10.1007/s10236-009-0226-1. 1, 2.1, 2.3, 3

J. Berntsen. *USERS GUIDE for a modesplit sigma-coordinate numerical ocean model. Version 4.1*. Department of Applied Mathematics, University of Bergen, Norway., http://math.uib.no/BOM/, 2004. 1, 2.1, 2.1

J. Berntsen and G. Furnes. Internal pressure errors in sigma-coordinate ocean models-sensitivity of the growth of the flow to the time stepping method and possible non-hydrostatic effects. *Cont. Shelf Res.*, 25:829–848, 2005. 1, 2.2

J. Berntsen, J. Xing, and G. Alendal. Assessment of non-hydrostatic ocean models using laboratory scale problems. *Cont. Shelf Res.*, 26:1433–1447, 2006. 1

J. Berntsen, J. Xing, and A. Davies. Numerical studies of internal waves at a sill: Sensibility to horizontal grid size and subgrid scale closure. *Cont. Shelf Res.*, 28:1376–1393, 2008. 1

J. Berntsen, J. Xing, and A.M. Davies. Numerical studies of flow over a sill: sensitivity of the non-hydrostatic effects to the grid size. *Ocean Dyn.*, 2009. doi:10.1007/s10236-009-0227-0. 4

D. Bourgault and D.E. Kelley. Wave-induced boundary mixing in a partially mixed estuary. *J. Mar. Res.*, 61:553–576, 2003. 3.1

V. Casulli. Semi-implicit finite difference methods for the two-dimensional shallow water equations. *J.Comput.Phys.*, 86:56–74, 1990. 2.2

A.M. Davies and J. Xing. Modelling processes influencing shelf edge currents, mixing, across shelf exchange, and sediment movement at the shelf edge. *Dyn. Atmos. Oceans*, 34:291–326, 2001. 1

D.M. Farmer. Observations of nonlinear internal waves in a lake. *J. Phys. Oceanogr.*, 8: 63–73, 1978. 1, 3

R. Ferrari and C. Wunsch. Ocean Circulation Kinetic Energy: Reservoirs, Sources, and Sinks. *Annu. Rev. Fluid Mech.*, 41:253–282, 2009. 1

A.E. Gill. *Atmosphere-Ocean Dynamics*. Academic Press, 1982. ISBN-0-12-283520-4. 1

J. Grue, A. Jensen, P.-O. Rusås, and J.K. Sveen. Properties of large-amplitude internal waves. *J.Fluid Mech.*, 380:257–278, 1999. 3.1

P. Hall and A.M. Davies. The influence of an irregular grid upon internal wave propagation. *Ocean Mod.*, 10:193–209, 2005. 1

N.S. Heaps and A.E. Ramsbottom. Wind effects on the water in a narrow two-layerd lake. *Philos. Trans. R. Soc. London*, 259:298–310, 1966. 1

Y. Heggelund, F. Vikebø, J. Berntsen, and G. Furnes. Hydrostatic and non-hydrostatic studies of gravitational adjustment over a slope. *Cont. Shelf Res.*, 24:2133–2148, 2004. 2.2

D.A. Horn, J. Imberger, and G.N. Ivey. The degeneration of large-scale interfacial gravity waves in lakes. *J. Fluid Mech.*, 434:181–207, 2001. 1, 3

J.M. Huthnance. Circulation, exchange and water masses at the ocean margin: the role of physical processes at the shelf edge. *Progr. Oceanogr.*, 35:353–431, 1995. 1

Y. Kanarska and V. Maderich. A non-hydrostatic numerical model for calculating free-surface stratified flows. *Ocean Dyn.*, 53:176–185, 2003. 1, 2.2

Y. Kanarska, A. Shchepetkin, and J-C. McWilliams. Algorithm for non-hydrostatic dynamics in the Regional Ocean Modeling System. *Ocean Mod.*, 18:143–174, 2007. 1, 2.2

E. Keilegavlen and J. Berntsen. Non-hydrostatic pressure in σ coordinate ocean models. *Ocean Mod.*, 28:240–249, 2009. 1, 2.2

P.K. Kundu. A two-dimensional model of inertial oscillations generated by a propagating wind field. *Journal od Physical Oceanography*, 16, 1986. 1

P.K. Kundu. *Fluid Mechanics*. Academic Press, 1990. 4

A. Mahadevan, J. Oliger, and R. Street. A Nonhydrostatic Mesoscale Ocean Model. Part I: Well posedness and scaling. *J. Phys. Oceanogr.*, 26:1868–1880, 1996a. 1

A. Mahadevan, J. Oliger, and R. Street. A Nonhydrostatic Mesoscale Ocean Model. Part II: Numerical implementation. *J. Phys. Oceanogr.*, 26:1881–1900, 1996b. 1

J. Marshall, C. Hill, L. Perelman, and A. Adcroft. Hydrostatic, quasi-hydrostatic, and nonhydrostatic ocean modeling. *J. Geophys. Res. [Oceans]*, 102(C3):5733–5752, 1997. 1, 2.2

E.A. Martinsen and H. Engedahl. Implementation and testing of a lateral boundary scheme as an open boundary condition in a barotropic ocean model. *Coastal Eng.*, 11:603–627, 1987. 2.3

H. Michallet and G.N. Ivey. Experiments on mixing due to internal solitary waves breaking on uniform slopes. *J. Geophys. Res. [Oceans]*, 104(C6):13467–13477, 1999. 3.1

J.N. Moum, D.M. Farmer, W.D. Smyth, K. Armi, and S. Vagle. Structure and Generation of Turbulence at Interfaces by Internal Solitary Waves Propagating Shoreward over the Continental Shelf. *J. Phys. Oceanogr.*, 33:2093–2112, 2003. 3.1

W.H. Munk and C. Wunsch. Abyssal recipes II: energetics of tidal and wind mixing. *Deep-Sea Research I*, 45:1978–2010, 1998. 1

E.D. Skyllingstad, W.D. Smyth, J.N. Moum, and H. Wijesekera. Upper-layer turbulence during a westerly wind burst: a comparison of large-eddy simulation results and microstructure measurements. *J. Phys. Oceanogr.*, 29:5–28, 1999. 1

Ø. Thiem and J. Berntsen. Numerical studies of large-amplitude internal waves shoaling and breaking at shelf slops. *Ocean Dyn.*, 2009. doi:10.1007/s10236-009-0220-7. 3.1

B.M. Wadzuk and B.R. Hodges. Hydrostatic and Non-hydrostatic Internal Wave Models. Technical Report CRWR Online Report 04-09, University of Texas at Austin, http://www.crwr.utexas.edu/online.shtml, 2004. 77p. 1

C. Wunsch and R. Ferrari. Vertical Mixing, Energy, and the General Circulation of the Oceans . *Annu. Rev. Fluid Mech.*, 36:281–314, 2004. 1

J. Xing and A.M. Davies. Processes influencing the non-linear interaction between inertial oscillations, near inertial internal waves and internal tides. *Geophys. Res. Lett.*, 29: 10.1029/2001GL014199, 2002. 1

J. Xing and A.M. Davies. Influence of coastal effects, bottom topography, stratification, wind period, and mixing upon the off shore profile of wind induced currents. *Geophys. Res. Lett.*, 108(C2,3052):doi:10.1029/2002JC001377, 2003. 1